Uneven crystallization of lead halide perovskite in the carbon-electrode based, low-temperature mesoscopic perovskite solar cells •

Qing Rong; De'en Guo; Jiao Ma; Siyuan Lin; Han Huang 💿 ; Deming Kong; Yongli Gao 💿 ; Conghua Zhou 🕿 📵



J. Appl. Phys. 132, 205303 (2022) https://doi.org/10.1063/5.0120065





CrossMark

Articles You May Be Interested In

SnO₂ modified mesoporous ZrO₂ as efficient electron-transport layer for carbon-electrode based, lowtemperature mesoscopic perovskite solar cells

Appl. Phys. Lett. (June 2022)

Influence of road unevenness on vehicle response

AIP Conference Proceedings (July 2018)

Molecular dynamics simulation of continuous nanoflow transport through the uneven wettability channel

AIP Advances (January 2018)

500 kHz or 8.5 GHz? And all the ranges in between.









Cite as: J. Appl. Phys. 132, 205303 (2022); doi: 10.1063/5.0120065 Submitted: 11 August 2022 · Accepted: 13 October 2022 · Published Online: 22 November 2022







Qing Rong,¹ De'en Guo,¹ Jiao Ma,¹ Siyuan Lin,¹ Han Huang,¹ D Deming Kong,¹ Yongli Gao,² D and Conghua Zhou^{1,a)}

AFFILIATIONS

¹Hunan Key Laboratory of Super-microstructure and Ultrafast Process, Hunan Key Laboratory of Nanophotonics and Devices, Institute of Super-microstructure and Ultrafast Process in Advanced Materials (ISUPAM), School of Physics and Electronics, Central South University, Changsha, Hunan 410083, People's Republic of China

²Department of Physics and Astronomy, University of Rochester, Rochester, New York 14627, USA

a)Author to whom correspondence should be addressed: chzhou@csu.edu.cn

ABSTRACT

Crystallization of perovskite is monitored in carbon-electrode based, low-temperature, mesoscopic perovskite solar cells. Crystallographic and morphological properties of the perovskite are examined through changes in the film thickness of carbon-electrode or the volume of perovskite precursor. It is observed that, when a relatively thin carbon-electrode or large volume of perovskite precursor is used, perovskite or large volume of perovskite precursor is used, perovskite or large volume of perovskite precursor is used, perovskite or large volume of perovskite precursor is used, perovskite or large volume of perovskite precursor is used, perovskite or large volume of perovskite precursor is used, perovskite or large volume of perovskite precursor is used, perovskite or large volume of perovskite precursor is used, perovskite or large volume of perovskite precursor is used, perovskite or large volume of perovskite precursor is used, perovskite or large volume of perovskite precursor is used, perovskite or large volume of perovskite precursor is used, perovskite or large volume of perovskite precursor is used, perovskite or large volume of perovskite precursor is used, perovskite or large volume of perovskite precursor is used, perovskite or large volume or larg crystallites mainly form on the device surface, leaving the bottom part of the device un-wetted. However, if a thicker carbon-electrode or less perovskite precursor is used, crystallization could be seen in the whole porous skeleton, and relative uniform distribution of perovskite crystallites is achieved. As such, uneven crystallization is observed. Such behavior is due to solvent evaporation on the surface, which facilitates nucleation processes on the surface, while retards crystallization on the bottom due to the Ostwald ripening effect. Charge transfer/ recombination processes and photo-to-electric power conversion properties are studied. As expected, uneven crystallization results in retarded charge transfer and increased risk of recombination, and poor power conversion efficiency, for example, ~3%. In contrast, uniform crystallization accelerates charge transfer and reduces recombination risk, and increases the efficiency to higher than 11% (AM1.5G, $100 \,\mathrm{mW/cm^2}$).

Published under an exclusive license by AIP Publishing. https://doi.org/10.1063/5.0120065

I. INTRODUCTION

Since 2009, huge success has been witnessed in perovskite solar cells (PSCs) and the power conversion efficiency (PCE) of the new photovoltaic technique has increased from 3.8% to 25.7%, though most of the high efficiencies relied on electrodes based on gold or silver. 1-5 Usage of metallic electrodes increases the cost. On the other hand, metal material is easily corroded by halide perovskite material, thus deteriorating device stability.^{6,7} Carbon-electrode based on graphite and carbon black is known by the advantages of low price, abundant reserves, inert chemical nature, and excellent conductivity. It has been widely used in daily life, like dry cells, and lithium cells. To reduce the risk of corrosion, carbon-electrode has also been applied in PSCs, leading to building a branch of carbonelectrode basing PSCs (shortened by CPSCs). During the past 9 years, several structures have been proposed such as embedded,8, quasi-planar/planar, 10-12 mesoscopic, 13-15 and so on. Among them, the mesoscopic structure (shortened by meso CPSCs) is unique for the triple mesoporous layer of "TiO2/ZrO2/carbon," with perovskite crystallites filling in the mesoporous skeleton. Since the pioneering work of Han et al. in 2003, PCE of such devices has increased from 6.64% to 18.82%, ¹⁷ though high temperature (~450 °C) procedure is adopted. To further reduce the fabrication cost of the meso CPSCs, low-temperature fabrication routines have been developed. For example, with the help of TiO₂-nanoparticle binding lowtemperature carbon-electrode, and vacuum-assisted perovskite crystallization, the fabrication temperature of meso CPSCs could be

lowered to <150 °C, and PCE of 12.29% and storage stability >220 days were reported in 2020.¹⁸ Recently, PCE of 13.37% was obtained by replacing the mesoporous electron-transport layer (ETL) from TiO₂ to SnO₂-modified ZrO₂ in the low-temperature CPSCs. ¹⁹ However, the efficiency of low-temperature CPSCs is still far behind that of metal-electrode basing devices, and, thus, it is quite essential to break down the bottleneck.

It is well-known that obtaining high quality perovskite crystallites is one of the key factors for high-performance PSCs. For example, rapid crystallization usually leads to concentrated grain boundaries in the perovskite film and a high density of defects, lowering down efficiency and stability of metal-electrode basing PSCs. 20,21 Similar behavior has also been depicted in meso CPSCs. To obtain better crystallization, Han et al. in 2020 proposed a strategy to control the evaporation rate of solvent, which upgraded the crystallization of perovskite in the mesoporous skeleton and raised the PCE to 16.26%.²² In 2021, by inhibiting a rapid nucleation of MAPbI₃, they further promoted the crystallization and moved the PCE up to 18.82%. 17 Besides, the crystallization process was observed to be affected by polarity, viscosity, and wettability of the solvent,²³ morphological properties of TiO₂,²⁴ graphite,^{25,26} and so on. Controlling the crystallization behavior plays a key role in obtaining high quality crystallites.

According to the unique structure of the meso CPSCs, the crystallization process of perovskite could be separated to four processes: precursor penetration, solvent evaporation, nucleation, and growth. Among these processes, "penetration" is always done at the initial wetting process, though it is affected by the wettability between the solution and mesoporous skeleton.²³ The other three processes are suggested to be highly "mixed." With solvent evaporating, nucleation could take place if super-saturation is reached; meanwhile, previously formed particles and nucleus could also find the opportunity to grow. As such, "solvent evaporation" provides the basic driving force for the last two processes, nucleation and growth. To manipulate the crystallization process, more attention should be paid to the evaporation process, like that done in previous reports. 17,22 Here in this paper, the crystallization of perovskite is monitored in low-temperature meso CPSCs through changes in the film thickness of carbon-electrode, and the volume of perovskite solution. As will be shown later, solvent evaporation could cause uneven crystallization of perovskite in the device, which affects the charge transfer and recombination, and hence, the power conversion properties of the devices. Controlling such uneven crystallization is found to be essential for efficient device fabrication.

II. EXPERIMENTAL

A. Material and reagent

Graphite (99.85%), zirconium oxide powder (ZrO2, 99%), ethanol (99.7%,) and acetone (99%), isopropyl alcohol (IPA), and tin (II) chloride dehydrate (SnO₂.2H₂O, 98%) were purchased from Sinopharm (Shanghai). Lead iodide (PbI2, 99%) and methylammonium iodide (CH₃NH₃I, MAI, 99%) were bought from Xi'an Polymer Light Technology Corp. Chitosan (CS, MW~30 000) were purchased from Macklin and used after dissolution. Carbon black (Ketjen), γ-butyrolactone (GBL, 99.9%, Aladdin), n-Butanol zirconium [Zr(OC₄H₉)₄, 80 wt. %, Macklin], and HOOC (CH₂)₄NH₃I (5-AVAI, 99%) were purchased from the domestic market and used as received. De-ionized water was prepared in the laboratory.

B. Material synthesis

SnO₂ quantum dots (SnO₂QDs) colloid (0.15 M) was prepared following the method described before. Typically, SnCl₂·2H₂O (1015 mg) and CH₄N₂S (335 mg) were dissolved in de-ionized water (30 ml), stirred for two days to form colloid, and then filtered before usage. Carbon paste was prepared by ball-milling 2 g graphite and 0.25 g carbon black in 20 ml alcohol for 24 h. 5 ml ZrO₂ colloid was added as an inorganic binder. ZrO2 suspension was prepared by ball-milling 3 g ZrO2 powder and 2 ml glycol in 20 ml alcohol for 24 h. Perovskite precursor was prepared by dissolving MAI (0.3975 g), PbI₂ (1.146 g), and 5-AVAI (0.03 g) in 2.7 ml GBL. The resultant concentration was 0.92 mol/l.

C. Device preparation

The mesoporous skeleton was fabricated by low-temperature procedures, as shown in Fig. 1. First, the FTO substrate was ultrasonically cleaned by de-ionized water, acetone, and IPA for 20 min each, dried in an oven, and then treated by UV/ozone for 20 min. A compact electron-transport layer (ETL) was prepared by spincoating SnO₂QDs colloid on FTO (3000 rpm) for 30 s and annealed at 150 °C for 1 h in open air. Porous ETL was prepared as follows: At first, the mesoporous ZrO_2 layer was prepared by spin-coating $\frac{80}{60}$ ZrO_2 suspension on the compact ETL (5000 rpm, 30 s) and $\frac{80}{60}$ annealed at 150 °C for 1 h. Then, one layer of SnO₂ was deposited by spin-coating diluted SnO₂QDs colloid (0.1 M) at 3000 rpm for $\frac{1}{8}$ 30 s and annealed at 150 °C for 1h again. After that, three more mesoporous ZrO_2 blocking layers were prepared by spin-coating $\frac{3}{5}$ (3000 rpm for 30 s) and annealing (150 °C for 1 h). Carbon-electrode was prepared by the doctor blading method, followed by annealing at 150 °C for 5 h in air. Film thickness of the electrode was controlled by tape layers. Finally, $45 \,\mu$ l perovskite precursor was imported to the mesoporous skeleton and heated at ~50 °C for 3 h in a vacuum oven. To study the effect of the film thickness of carbon-electrode on the crystallization behavior of perovskite, the volume of perovskite precursor was kept at 45μ l, in which four kinds of film thickness or \sim 5, \sim 10, \sim 13, and \sim 17 μ m were applied by varying the tape layers from 1 to 4. Surface profiling property and the relationship between the film thickness and tape layers are shown in Fig. S1 in the supplementary material. In contrast, in order to study the effect of the volume of perovskite precursor on the crystallization behavior, different volumes like 10, 20, and 40 µl were used, while the carbon-electrode was kept at a thickness of about $5 \mu m$.

D. Material characterization and device performance evaluation

Cross-sectional and surface morphological properties, as well as the crystallographic properties of the low-temperature meso CPSCs were characterized by scanning electron microscopy (SEM, TESCAN MIRA3 IMU) and x-ray diffraction (XRD, D8 Advance,

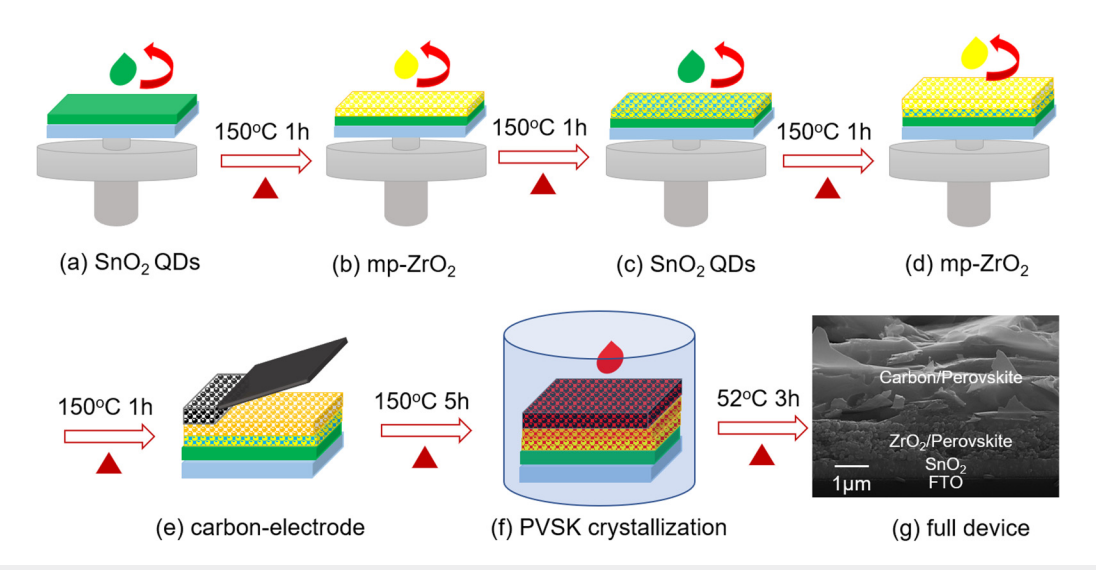


FIG. 1. (a)-(f) Schematic for the preparation of low-temperature meso CPSCs. (g) Typical cross-sectional SEM image of the resulted low-temperature device.

Bruker), respectively. Specific surface area and pore size distribution were measured by Monosorb direct reading specific surface area analyzer (BET, Quadrasorb SI-3MP). The power conversion efficiency of devices was tested under simulated sunlight (ENLITECH SS-F7-3A, AM 1.5G, light intensity was calibrated to be 100 mW/cm²). Current density-voltage (JV) curves were recorded by a digital source-meter (Model 2400, Keithley Inc.). Impedance spectroscopy (IS) was performed on an electrochemical workstation (CHI 660D, Chenhua) under illumination (AM 1.5G, 100 mW/cm²) in the frequency range of 10⁴-10⁶ Hz. The obtained Nyquist plots were fitted by home-made software. Transient photovoltage/photocurrent (TPV/TPC) decay curves were recorded using a home-made system including a digital oscilloscope (DSO-X 3104A, Keysight) and N2 laser (NL100, 337 nm, Stanford). During TPV measurements, a background open-circuit voltage (VOC) of about 930 mV was generated by background illumination, and a perturbed voltage (ΔV_{oc}) of about 5% of the background voltage was generated by the laser pulse.

III. RESULTS AND DISCUSSION

A. Uneven crystallization of lead halide perovskite in the low-temperature meso CPSCs

Preparation procedure of the low-temperature meso CPSCs is schematically shown in Fig. 1(a)-1(f). All the procedures are done in a temperature of 150 °C or lower. A typical cross-sectional SEM image of a full device is shown in Fig. 1(g).

Crystallization behavior of the perovskite material is studied by monitoring the morphological and crystallographic properties. To study the effect of film thickness of the carbon-electrode on crystallization, the thickness is changed, while the volume of the perovskite solution is kept the same. Figure 2 shows SEM images of both surface and cross section of low-temperature devices, as well

as the element distribution properties. For comparison, a bare skeleton is examined.

As shown in Figs. 2(a) and 2(f), before perovskite loading, a relative smooth surface is observed; meanwhile, a layered structure is depicted, according to the cross-sectional image and the related element distribution of Sn, Zr, and C. However, loose packing is esen in the carbon-electrode layer. Then, after the perovskite material is leaded, morphological property changes on both surface and rial is loaded, morphological property changes on both surface and cross section. As shown in Fig. 2(b), a rough surface is obtained. Concentrated pyramids with a size of several micrometers could be $\vec{\omega}$ seen. Such pyramids belong to the lead halide perovskite, as $\frac{1}{100}$ reflected by the element distribution and following XRD studies. For example, from the inset of Fig. 2(b), one can see a concentrated distribution of Pb and I on the device surface. Meanwhile, from the following XRD studies [Fig. 4(a)], one can see that perovskite crystallization has taken place. On the other hand, perovskite loading also changes the cross-sectional structure of the device. The carbon-electrode region tends to be condensed, which is due to perovskite loading. However, perovskite material only fills the carbon-electrode region, leaving the bottom part less-wetted, as reflected by element distribution maps on the right-hand side of Fig. 2(g). Photo image observation comes with a similar result. When taking a photo from the bottom side, the "bare" region could be clearly observed, as shown in the inset of Fig. 2(g). Therefore, at such a case or when the carbon-electrode is relatively thin (\sim 5 μ m), perovskite crystallization mainly takes place at the top part of the device. This is what we name as "uneven crystallization." Such behavior retards the power conversion processes, as will be shown later. However, after the carbon-electrode gets thicker, the uneven behavior tends to be reduced. As seen in Fig. 2(c), fewer pyramids are left on the device surface when the film thickness increases to $\sim 10 \,\mu \text{m}$ for the carbon-electrode, even though the same volume (45 µl) of perovskite precursor is used. However, from Fig. 2(h) one can see that elements of Pb and I could

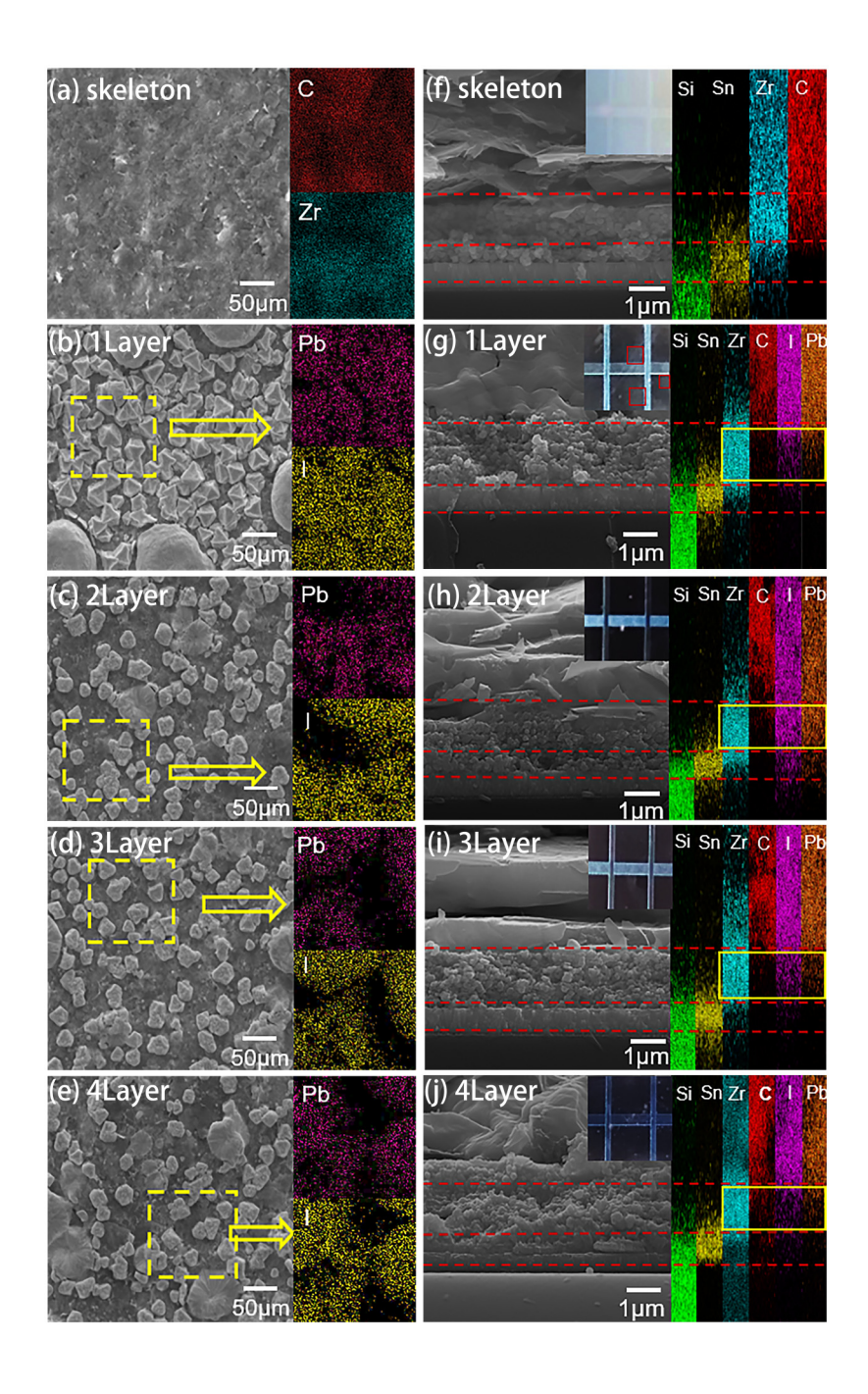


FIG. 2. SEM images of the surface (left) and cross section (right) of low-temperature mesoscopic perovskite solar cells (meso CPSCs) prepared with different thicknesses of the carbon-electrode controlled by tape layers. (a) and (f) Porous skeleton (before perovskite is loaded, the carbon-electrode is $\sim\!\!5\,\mu\mathrm{m}$ in thickness, according to one-layer tape); (b) and (g) one-layer (after perovskite loading, so are the following three cases); (c) and (h) two-layer; (d) and (i) three-layer; and (e) and (j) four-layer. Corresponding element distribution mapping (EDS) is shown on the right side of each SEM image (both surface and cross section). An optical image of the device (taken on the glass side) is embedded inside the right column cross-sectional SEM figures.

distribute in the middle meso- ZrO_2 layer, even reaching the bottom of the SnO_2 layer. Photo image observation comes out with a similar result. The bottom of the mesoporous skeleton could be wetted by the perovskite material, as reflected by the photo presented in the inset of Fig. 2(h). As a result, uniform distribution has been achieved just by increasing the film thickness of the carbon electrodes. According to the unique device structure, strengthened contact between the active layer and both top carbon-

electrode and bottom ETL is essential for power conversion. Such features will be reflected later during the performance tests. In more, a further increase in the film thickness of carbon-electrode comes out with similar behavior for the distribution of perovskite. However, as the film thickness increases to $\sim 17\,\mu\text{m}$, it becomes relatively difficult for perovskite to penetrate into the bottom part of the device. As reflected in Fig. 2(j), the intensity of Pb/I signals drops quickly as it gets close to the bottom SnO₂ layer. Such

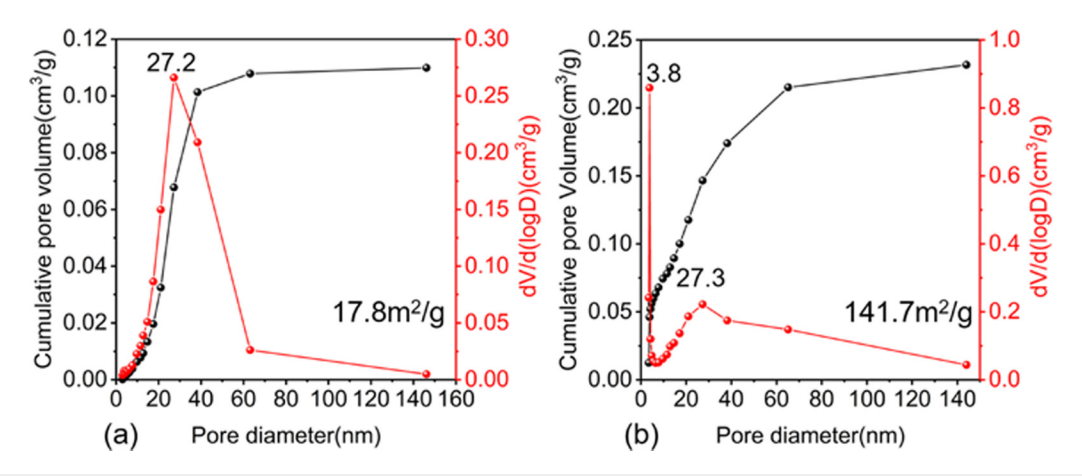


FIG. 3. Pore size distribution recorded from BET test. (a) meso-ZrO₂ film and (b) carbon-electrode. The insets are the specific surface area.

behavior might be ascribed to the increased capillary effect. To show more details, pore size distribution and specific surface area of meso-ZrO $_2$ and carbon-electrode are tested. As is shown in Fig. 3, the pore size distributes around 27.2 nm for meso-ZrO $_2$, while around 3.8 nm (major peak) and 27.3 nm (minor peak) for the carbon-electrode. In addition, meso-ZrO $_2$ shows a specific surface area of 17.8 m 2 /g, while the carbon-electrode comes out with 141.7 m 2 /g. Obviously, the carbon-electrode shows a higher specific surface area but a smaller pore size. Such a structure will cause a heavy capillary effect, which could affect the

infiltration process of the perovskite precursor, and, thus, the crystallization.

Crystallographic property of the perovskite is examined by XRD using fresh devices that are picked after the crystallization of the perovskite. Perovskite phase is observed in all four kinds of film thicknesses. Concretely, peaks at around 14.19°, 20.12°, 23.58°, 28.48°, 31.84°, 40.60°, and 43.17° could be marked to facets of (110), (112), (111), (004), (310), (202), and (212) of the perovskite, respectively. Since perovskite tends to form at the device surface, of the reduce the effect of the surface perovskite layer, XRD is

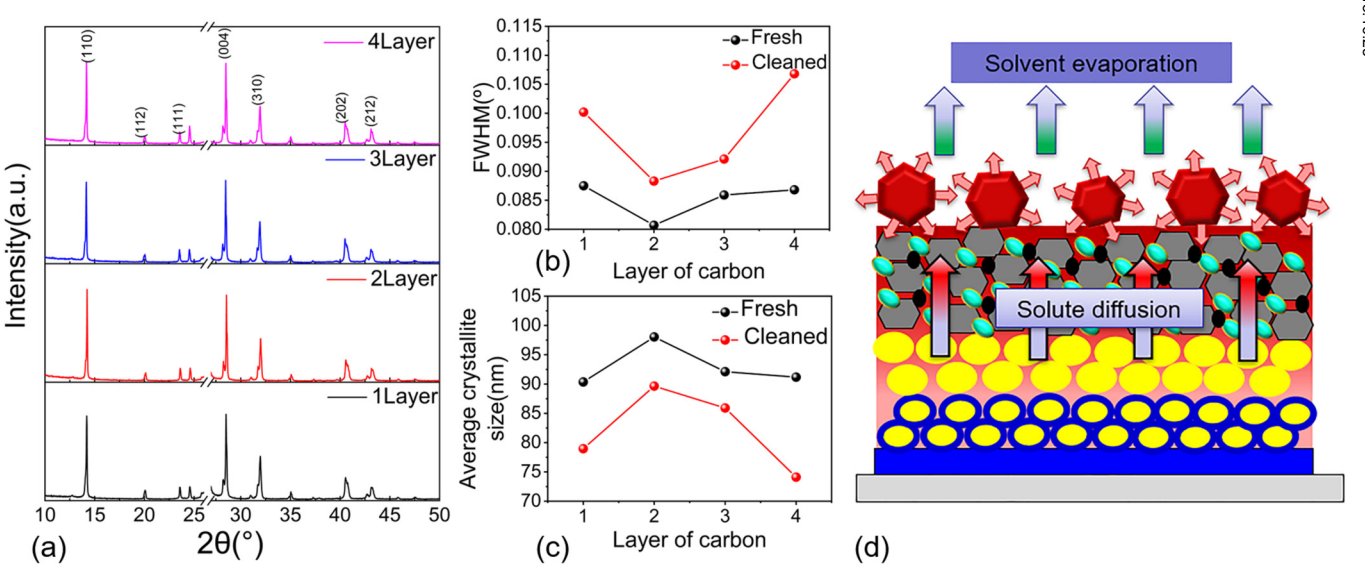


FIG. 4. (a) XRD patterns of the low-temperature device assembled from the carbon-electrode with varied film thickness. (b) 2-theta at full-width at half-magnitude (2θ-FWHM) value of facet (110) of perovskite. (c) Average crystallite size of perovskite derived from Scherrer's equation. (d) Schematic for the evaporation caused uneven distribution.

re-performed after the surface layer is brushed by tapes. The detailed XRD patterns are shown in Fig. S3 in the supplementary material. For a meaningful comparison, 2-theta full-width at half-magnitude (2θ -FWHM) of peak (110) is picked. Corresponding results are shown in Fig. 4(b). As the film thickness of the carbon-electrode increases, the 2θ -FWHM decreases at first and then increases. Similar behavior is observed for the brushed devices, but a relatively larger 2θ -FWHM is obtained. Average crystallite size of the perovskite is calculated according to Scherer's formula, quoted as (1),

$$D = \frac{k\lambda}{\beta \cos \theta},\tag{1}$$

where k is the Scherrer constant, noted as 0.89; λ is the x-ray wavelength, for Cu target, it is 0.154 nm; β is 2θ -FWHM value but recorded with the unit of "rad;" θ is the diffraction angle; and D is the average crystallite size. As shown in Fig. 4(c), when the carbon-

electrode gets thicker, an inverse trend is obtained for the average crystallite size. It becomes larger at first and then turns to be smaller. As a result, the carbon-electrode has affected the crystallization of the perovskite. The relatively smaller crystallite size obtained at the one-layer case (\sim 5 μ m in thickness) is likely due to the fast nucleation behavior on the solution surface. When the carbon-electrode is relatively thin, void space in the mesoscopic skeleton is not enough to hold the solution that is imported; thus the solution is easy to be left on the surface. Due to the preferred solvent evaporation on the surface, nucleation is easy to happen on the surface layer of the perovskite precursor.²⁷ Accordingly, a relatively small crystallite size is obtained. As the carbon-electrode gets thicker, less volume of precursor remains on the surface. The evaporation rate could be slowed down due to the confinement effect brought by the mesoporous structure of the skeleton, which facilitates crystallite growth and, thus, increases the crystallite size. Such behavior is similar to that observed by Han et al. in evaporationcontrolling experiment. 17,22 However, as the carbon-electrode gets

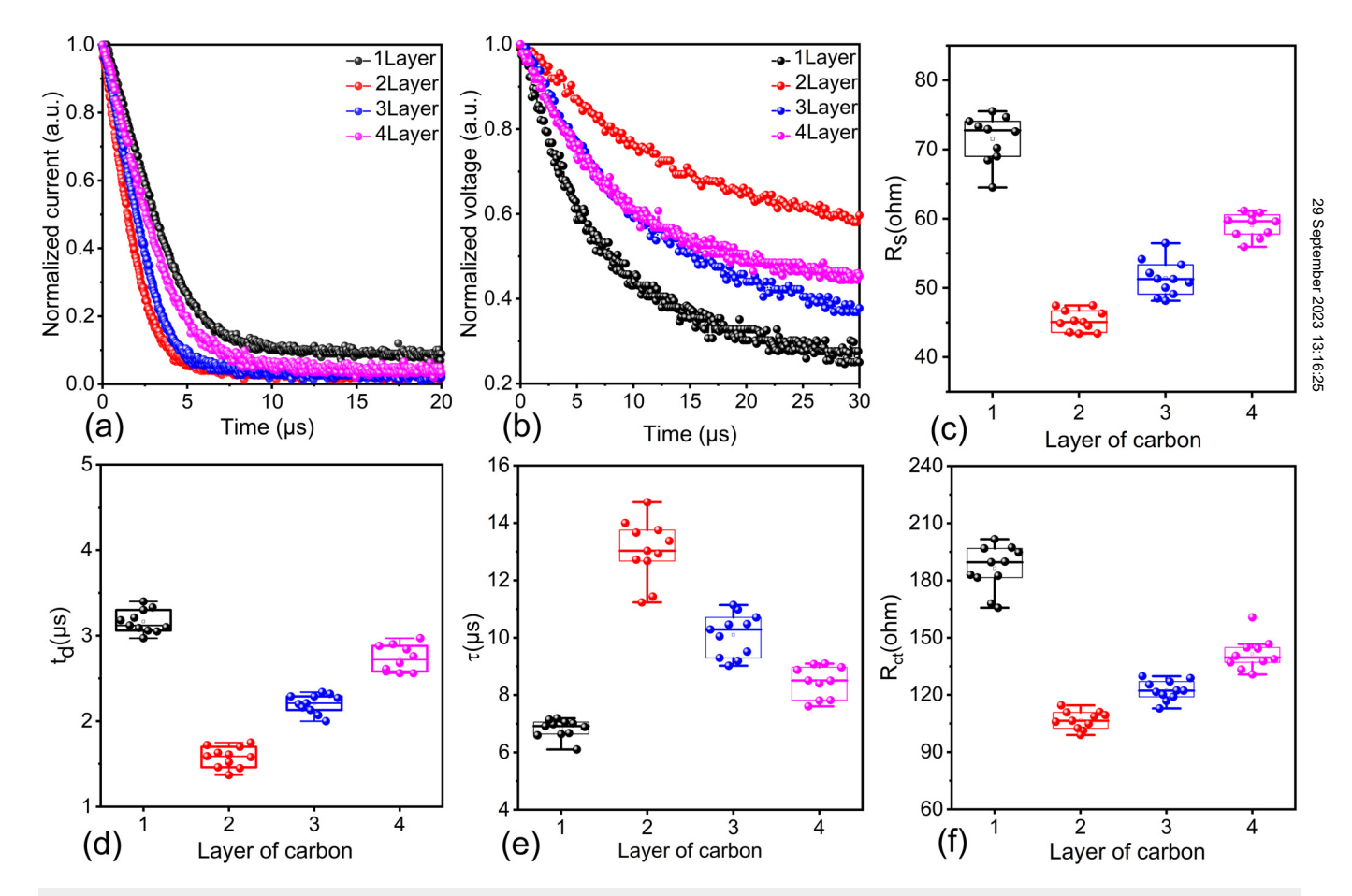


FIG. 5. Effect of the film thickness of the carbon-electrode on charge transfer and recombination kinetics. (a) and (b) Transient photocurrent/photovoltage (TPC/TPV) decay curves; (d) and (e) transition-time (t_d) and lifetime (τ) of photogenerated carriers fitted from the TPC/TPV decay curves; and (c) and (f) series resistance (R_s) and charge transfer resistance (R_{cl}) picked from Nyquist plots in the impedance spectroscope study.

to be too thick, an incomplete filling could take place, which retards crystallization and leads to smaller perovskite crystallites. In such a case, increasing the concentration of the solution was found to be helpful for crystallization. ²⁸ On the other hand, after the device surface is brushed by tapes, the average crystallite size decreases by about 10 nm for all four cases. Such a phenomenon implies that better crystallization takes place on the device surface, since there is less confinement like that in the mesoporous skeleton.

According to the above studies, it tends to show that when the carbon-electrode is relatively thin or the volume of perovskite precursor is relatively large, solvent evaporation could cause fast nucleation on the surface. The formed nuclei on the surface could take advantage to coarsen. According to the Ostwald ripening theory, the growth of these nuclei could extract solute from perovskite precursor stored by the bottom part of the device. Such a process leads to the uneven crystallization of perovskite. Anyhow, one may suppose the possible effect of hydrophobilicity on the uneven crystallization behavior. To make it clear, we tested the water contact angle of mesoporous frameworks with different carbon film

thicknesses. As is shown in Fig. S2 in the supplementary material, a one-layer carbon-electrode shows a contact angle of 29.3°, while a two-layer comes out with a contact angle of 43.5°, three-layer and four-layer with 47.8° and 50.2°, respectively. As a result, it becomes relatively hydrophilic when the carbon-electrode becomes thinner. Such a phenomenon also implies that the "uneven crystallization behavior" observed in the 1-layer case is not caused by the hydrophobicity of the mesoporous skeleton. To help the understanding of this interesting behavior, a schematic is shown in Fig. 4(d). Such a mechanism could well tell the cause of the above observations.

B. Impact of the uneven crystallization on power conversion properties

Charge extraction and recombination behavior of the low-temperature meso CPSCs are studied, with a combination of transient photocurrent/photovoltage (TPC/TPV) decay curves. Typical TPC/TPV decay curves are shown in Figs. 5(a) and 5(b), respectively. Transition-time (t_d) and lifetime (τ) of photogenerated carriers in devices are fitted from the TPC/TPV decay curves. The fitted

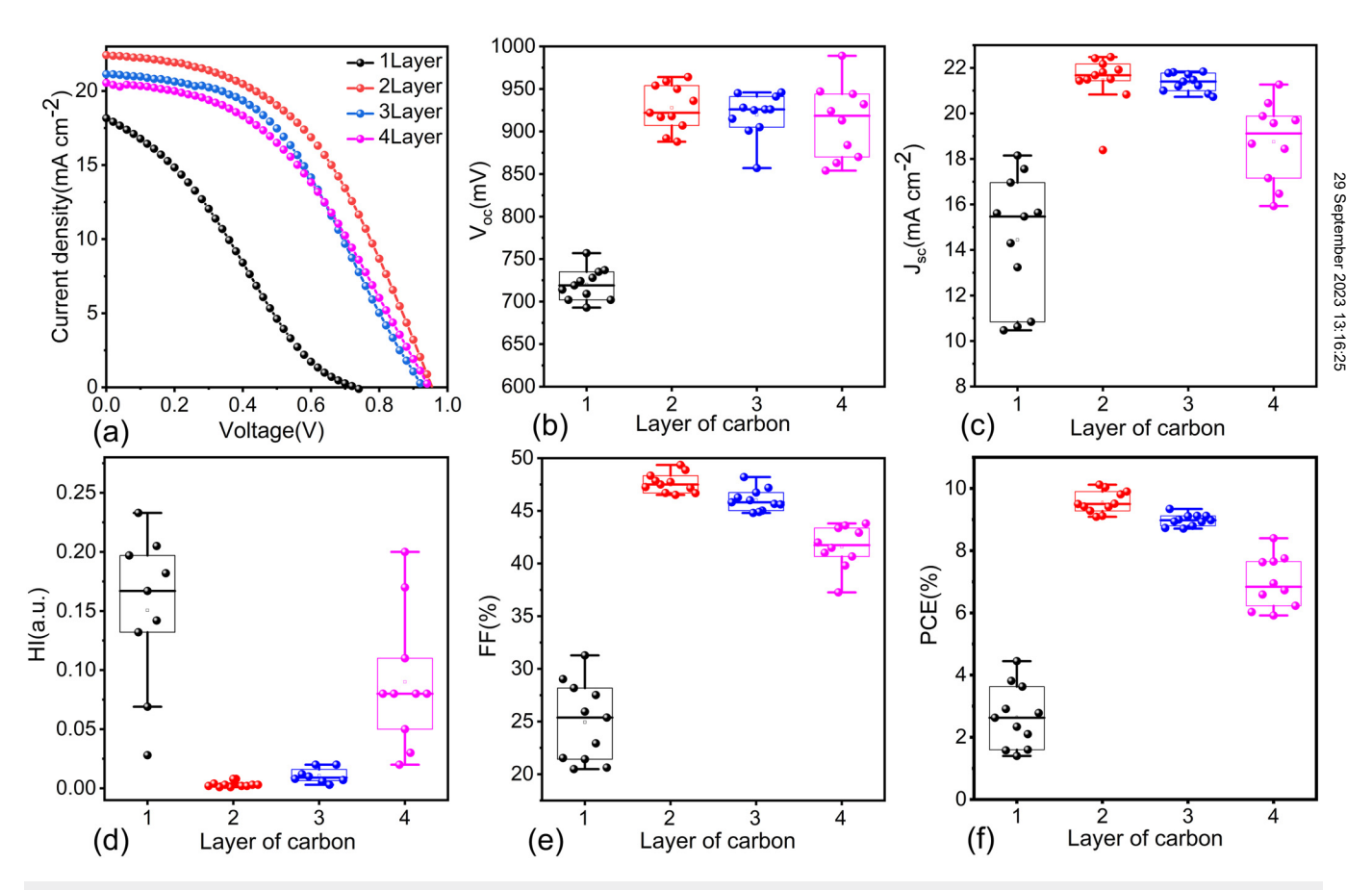


FIG. 6. (a) Typical current density–voltage (JV) curves (reverse scans) of the low-temperature devices (tested under simulated illumination of AM 1.5G, 100 mW/cm², with a test area of 0.0514 cm²). Statistics on performance parameters (reverse scan) of the low-temperature meso CPSCs assembled from the carbon-electrode with different film thicknesses (varied by layers of tapes in the doctoral blading method): (b) V_{oc} , (c) J_{sc} , (e) F_F , and (f) PCE. (d) Hysteresis index of devices.

results are shown in Figs. 5(d) and 5(e), respectively. It could be seen that when the carbon-electrode is about $5 \mu m$ (1-layer tape), the transition-time (t_d) is 3.18 $(\pm 0.35) \mu s$. As the thickness increases to ~10 μ m (two-layer tapes), it decreases to 1.87 (±0.27) μ s. Further increment in thickness brings an increase in the transition-time. For example, it is 2.48 (± 0.21) μ s for the three-layer and 2.87 $(\pm 0.32) \mu s$ for the four-layer cases, respectively. As for the lifetime (τ) , it is 7.05 $(\pm 0.67) \mu s$ at the one-layer case $(\sim 5 \mu m)$, then rising to 13.66 (± 0.39) μ s at the two-layer case ($\sim 10 \,\mu$ m). However, a further increase in tape layers observes shrinks in the lifetime. It is wellknown that solar cells are rate-determined devices. They are sensitive to charge transfer/recombination dynamics. Shorter transition-time (t_d) and prolonged lifetime (τ) are helpful for the power conversion process. The above observation relates closely to the crystallization behavior of perovskite in the low-temperature CPSCs. When the carbon-electrode is relatively thin ($\sim 5 \mu m$), charge extraction is slowed down due to the incomplete filling of the active layer (or the poor contact between perovskite and bottom ETL). After the carbon-electrode becomes thicker ($\sim 10 \,\mu m$ or more), perovskite crystallization becomes uniform, and the contact is strengthened between the active layer and bottom ETL. As a result, the extraction process is favored, and a shorter transitiontime (t_d) is harvested. In contrast, when charge extraction is retarded, recombination is more likely to happen, thus shorter lifetime (τ) is seen in the one-layer case. After charge extraction is accelerated, recombination is slowed down; thus longer lifetime (τ) is obtained. Similar behavior is observed in impedance spectroscopy (IS) measurements. Typical Nyquist plots are shown in Fig. S4 in the supplementary material. Then, series resistance (R_s) and charge transfer resistance (R_{ct}) are picked from the plots, and are shown in Figs. 5(c) and 5(f), respectively. When the one-layer tape is used ($\sim 5 \,\mu \text{m}$ for the carbon-electrode), R_s is 74.42 $(\pm 10.21) \Omega$, but drops to 45.25 $(\pm 3.82) \Omega$ at the two-layer case (\sim 10 μ m), although rises again after the thickness of the carbonelectrode increase. As for R_{ct} , it is 189.9 (±24.2) Ω at first, then decreases to 108.7 (±9.8) Ω after the thickness rises to ~10 μ m (two-layer tape), though it elevates again after the carbon-electrode becomes thicker. In fact, these two resistances evolve in parallel with each other. Again, the reduced value at moderate film thickness (\sim 10 μ m) is ascribed to the improved distribution of the perovskite in the skeleton, and the strengthened contact between the active layer and bottom ETL, like that observed before. 18,19 As a result, uneven crystallization retards charge transfer while increasing recombination risk.

Uneven crystallization could bring an obvious impact on the power conversion processes. As shown in Fig. 6(a), when the carbon-electrode is relatively thin ($\sim 5 \mu m$), or uneven crystallization happens, a "S-shape" characteristic appears in the JV curve, which means a heavy barrier exists in the device. According to the above studies and also a previous study, 19 this behavior is due to the incomplete contact between perovskite and bottom ETL. Then, as perovskite crystallization becomes uniform, the contact is strengthened, and normal J-V curves appear. Performance parameters are picked from the J-V curves, including open-circuit voltage (V_{oc}) , short-circuit current density (J_{sc}) , filling factor (FF), as well the PCE, which is shown in Figs. 6(b), 6(c), 6(e), and 6(f), respectively. Obviously, as uneven crystallization dominates, V_{oc} of 728 (± 32) mV, I_{sc} of 15.82 (± 3.89) mA/cm², FF of 25.47 (± 7.45) %, and PCE of 2.93 (±1.36)% are obtained. After crystallization becomes more uniform, V_{oc} of 925 (±22.43) mV, J_{sc} of 21.42(±1.12) mA/cm², FF of 47.26(±3.58)%, and PCE of 9.69 (±0.74)% are obtained. Such a phenomenon coincides well with the charge transfer/recombination studies. The accelerated charge extraction and the retarded charge recombination are helpful for device efficiencies. Hysteresis index (HI) is also collected according to formula (2):

$$HI = \frac{PCE^+ - PCE^-}{PCE^+ + PCE^-},\tag{2}$$

where PCE+/PCE- represents PCE recorded from reverse/forward scans, respectively. Clearly, relatively higher HI is observed when uneven crystallization behavior takes place, while smaller HI dominates as the uneven behavior shrinks. Indeed, the HI is sensitive to the crystallization quality of the perovskite particles. Crystal defects usually cause heavy HI due to ion migration.^{29,30} According to Fig. 2, relatively smaller crystallites are observed when uneven crystallization dominates, leading to higher HI. As such, reducing uneven crystallization is also helpful to reduce HI.

Storage stability of devices is monitored by keeping the devices (without encapsulation) in open air (dark) with a relative humidity of about 35%-40%. As shown in Fig. 7, when the carbon film thickness is $\sim 5 \,\mu \text{m}$ (one-layer tape), less shrinking is observed for the original 140 days, but then drops quickly. Similar behavior could be seen for devices with a film thickness of $\sim 17 \,\mu \text{m}$ (fourlayer tapes). Such a phenomenon is related to uneven crystallization $\frac{\omega}{2}$ behavior. However, in the other two cases, when the film thickness is about $10-13 \,\mu\mathrm{m}$ (two or three-layer tapes), prolonged stability is observed, even after the devices were stored for nearly half a year. S The relative poorer stability in one-layer and four-layer cases is $\frac{1}{\omega}$ related to the crystallization behavior of perovskite in low-

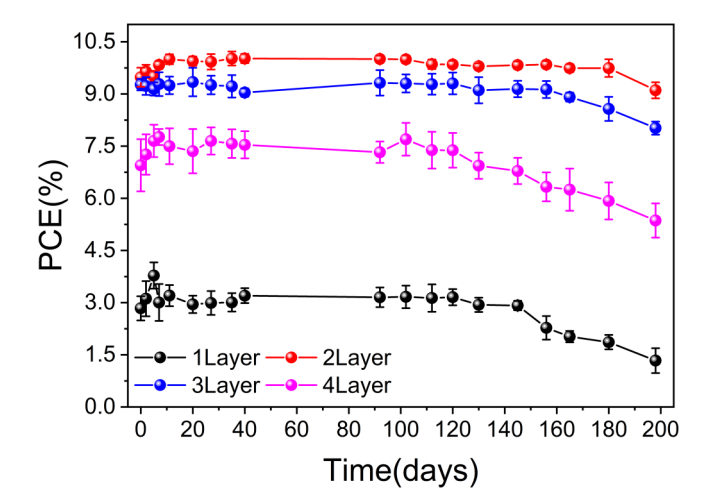


FIG. 7. Storage-stability test on the low-temperature meso CPSCs assembled with carbon-electrode of different film thicknesses (relative humidity of 35%-40%).

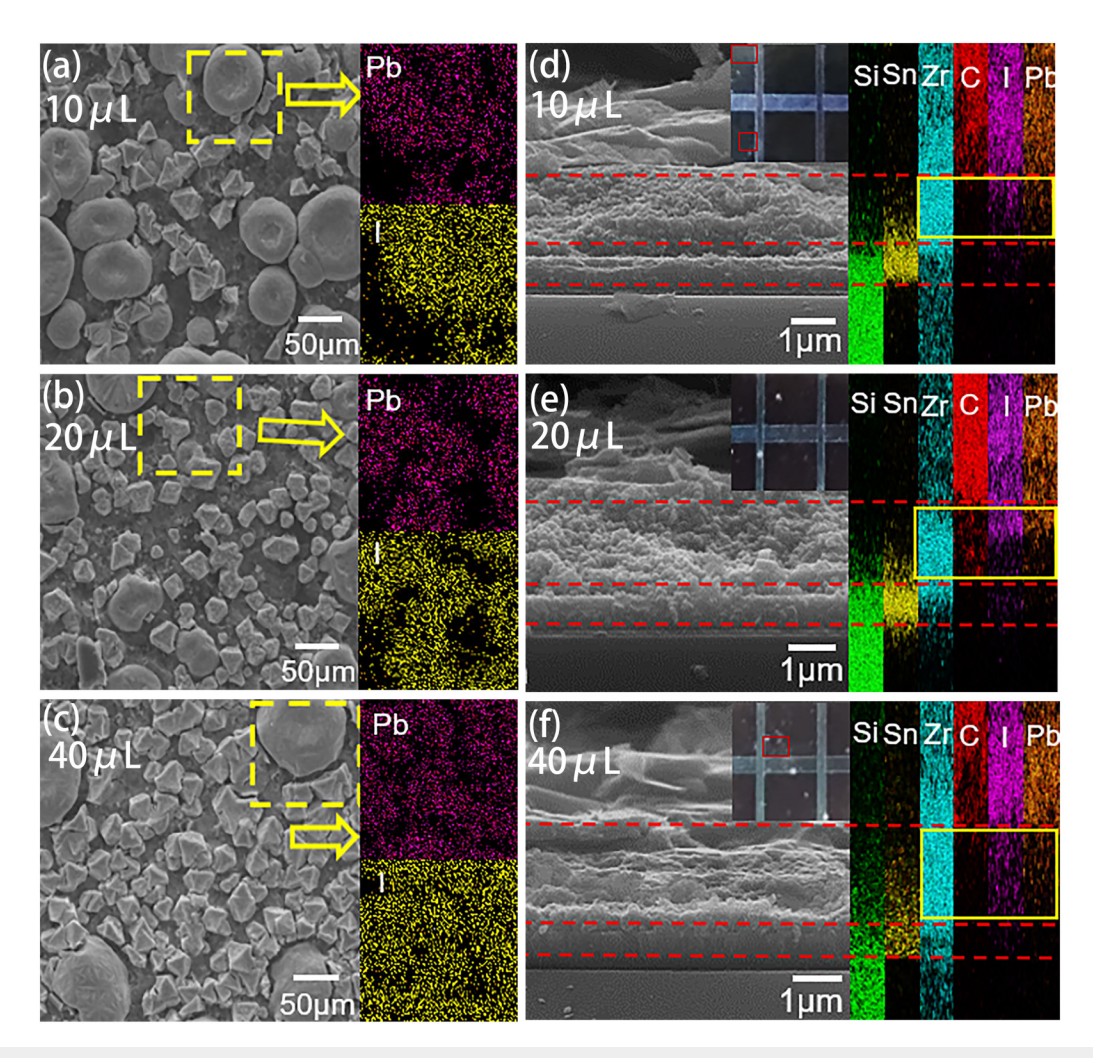


FIG. 8. SEM images of surface (left) and cross section (right) of low-temperature meso CPSCs prepared with different volumes of perovskite solution (μ): (a) and (d) 10, (b) and (e) 20, and (c) and (f) 40 μl. Corresponding element distribution mapping (EDS) is shown on the right side of each SEM image (both surface and cross section). Optical image of the device (taken on the glass side) is embedded inside the right column cross-sectional SEM figures. The carbon-electrode is ~5 μm in thickness.

temperature devices. As stated above, when the carbon-electrode is relatively thin, perovskite crystallites tend to form at the surface layer of the device. Since perovskite is highly hydrophilic, it could be easily dissolved by moisture, leading to relatively poor storage stability.

C. Effect of the volume of perovskite precursor and hydrophilicity of meso-ZrO₂ on the uneven crystallization behavior

Uneven crystallization is also observed when changing the volume of the perovskite precursor during device fabrication. According to the above experiment, the film thickness is kept at \sim 5 μ m, and precursor volume is chosen to be 10, 20, and 40 μ l, respectively, since the above experiment has already shown that "45 μ l" caused "uneven crystallization." Figure 8 shows the SEM

cross section and corresponding element distribution maps of low-temperature meso CPSCs. When the volume is 10 or $40\,\mu$ l, concentrated pyramids are seen on the device surface, while a void area exists at the device bottom when taking photos from the glass side. According to the above discussions, it could be well deduced that uneven crystallization behavior appears in these two cases. Similarly, the behavior also affects the charge transfer/recombination process. As shown in Fig. S5 in the supplementary material, when uneven crystallization happens, a relative longer charge transition-time (t_d) and shorter lifetime (τ) are obtained; meanwhile, larger residential resistance (R_s) and charge transfer resistance (R_{ct}) are observed. As such, charge transfer is retarded, and recombination is favored when uneven crystallization takes place. Accordingly, power conversion property of the low-temperature device is also affected. As shown in Fig. S6 in the supplementary

material, smaller performance parameters are obtained when uneven crystallization behavior appears.

It is also worth noting that the observed behavior is different from the previous study in the high-temperature meso CPSCs, where the film thickness of the carbon-electrode was also changed.³¹ For example, even when the carbon-electrode was as thin as $5 \mu m$, the perovskite crystallite could form in the mesoporous skeleton, reaching the bottom of the device. And thus, the uneven crystallization behavior was not met in the hightemperature device. Such a phenomenon might relate to the difference in the structure of the skeleton. For example, in previous high-temperature meso CPSCs, mesoporous TiO2 was used as the mesoporous ETL; while in the current work, such a layer is replaced by SnO2-modified ZrO2. TiO2 is known by its high surface activity; thus, might be more convenient for the loading of perovskite crystallites.³² However, due to the high UV-sensitivity and related photo-catalysis effect, in this work and previous work, TiO₂ is replaced.¹⁹ On the other hand, the uneven crystallization behavior might also be related to the hydrophilicity of the skeleton.

Hydrophobicity could make such a behavior easier to happen, while improving the hydrophilicity is helpful to reduce the uneven crystallization effect. As is shown in Fig. S7 in the supplementary material, adding chitosan (5 mg/ml) into ZrO2 could improve the wettability of meso-ZrO₂. In fact, another group of experiments is added by incorporating Chitosan in ZrO2, after which the effect of the thickness of carbon-electrode on the crystallization behavior, and, thus, the power conversion properties are examined. Interestingly, similar behavior is observed. SEM and EDS studies are performed. Two typical samples are picked for comparison. One is the one-layer carbon-electrode and the other is the two-layer case; the results are shown in Fig. S8 in the supplementary material. It could be seen that uneven crystallization also happens in the one-layer case, while the two-layer comes out with improvement. As a result, the uneven crystallization behavior could be well repeated. Such behavior also affects the power conversion properties. Typical JV curves and corresponding performance parameters are collected in Fig. S9 in the supplementary material. Again, the two-layer carbon-electrode shows the best device efficiency, while one layer is the worst. But due to the improved hydrophilicity in meso-ZrO2, the PCE is slightly upgraded to 11.61%.

IV. CONCLUSION

In conclusion, uneven crystallization is observed in the lowtemperature meso CPSCs, which is due to the preferred solvent evaporation on the surface. Such behavior leads to a relatively poorer crystal quality of perovskite and also weak contact between the active layer and bottom ETL, which retards power conversion processes. Reducing uneven crystallization is then essential for the fabrication of efficient and stable low-temperature meso CPSCs.

SUPPLEMENTARY MATERIAL

See the supplementary material for the carbon film thickness test (Fig. S1), water contact angle test of the mesoporous skeleton (Fig. S2), XRD pattern (Fig. S3), EIS test (Fig. S4), effect of precursor volume on charge transfer and recombination kinetics (Fig. S5), effect of precursor volume on performance parameters (Fig. S6),

optical images before and after riboglycan doping (Fig. S7), SEM characterization after adding chitosan in meso- ZrO_2 (Fig. S8), and typical JV curves and performance parameters of devices with the incorporation of chitosan in meso- ZrO_2 (Fig. S9).

ACKNOWLEDGMENTS

C. Zhou thanks the financial support of the National Natural Science Foundation of China (NSFC, No. 61774170) and Natural Science Foundation of Hunan Province (No. 2020JJ4759), and the Innovation-Driven Project of Central South University (No. 2020CX006). Y. Gao acknowledges support from the National Science Foundation, United States (NSF, No. DMR-1903962). Q. Rong acknowledges the financial support from the Fundamental Research Funds for the Central South University (No. 2022ZZTS0675).

AUTHOR DECLARATIONS

Conflict of Interest

The authors declare no conflict of interest.

Author Contributions

Qing Rong: Data curation (lead); Formal analysis (equal); Investigation (lead); Methodology (equal); Writing – original draft (lead); Writing – review & editing (equal). De'en Guo: Methodology (equal). Jiao Ma: Methodology (equal). Siyuan Lin: Methodology (equal). Han Huang: Methodology (equal). Deming Kong: Methodology (equal). Yongli Gao: Writing – review & editing (equal). Conghua Zhou: Conceptualization (lead); Supervision (lead); Writing – review & editing (equal).

DATA AVAILABILITY

The data that support the findings of this study are available within the article and its supplementary material.

REFERENCES

¹A. Kojima, K. Teshima, Y. Shirai, and T. Miyasaka, "Organometal halide perovskites as visible-light sensitizers for photovoltaic cells," J. Am. Chem. Soc. 131(17), 6050 (2009).

²C. T. Zuo, H. J. Bolink, H. W. Han, J. S. Huang, D. Cahen, and L. M. Ding, "Advances in perovskite solar cells," Adv. Sci. 3(7), 1500324 (2016).

³C. Q. Ma and N. G. Park, "A realistic methodology for 30% efficient perovskite solar cells," Chem 6(6), 1254–1264 (2020).

⁴J. J. Yoo, G. Seo, M. R. Chua, T. G. Park, Y. L. Lu, F. Rotermund, Y. K. Kim, C. S. Moon, N. J. Jeon, J. P. Correa-Baena, V. Bulovic, S. S. Shin, M. G. Bawendi, and J. Seo, "Efficient perovskite solar cells via improved carrier management," Nature 590(7847), 587–593 (2021).

⁵H. Min, D. Lee, J. Kim, G. Kim, K. S. Lee, J. Kim, M. J. Paik, Y. K. Kim, K. S. Kim, M. G. Kim, T. J. Shin, and S. I. Seok, "Perovskite solar cells with atomically coherent interlayers on SnO₂ electrodes," Nature 598(7881), 444 (2021).

⁶Y. Kato, L. K. Ono, M. V. Lee, S. H. Wang, S. R. Raga, and Y. B. Qi, "Silver iodide formation in methyl ammonium lead iodide perovskite solar cells with silver top electrodes," Adv. Mater. Interfaces 2(13), 1500195 (2015).

⁷S. Svanstrom, T. J. Jacobsson, G. Boschloo, E. M. J. Johansson, H. Rensmo, and U. B. Cappel, "Degradation mechanism of silver metal deposited on lead halide perovskites," ACS Appl. Mater. Interfaces 12(6), 7212–7221 (2020).

- ⁸Z. H. Wei, K. Y. Yan, H. N. Chen, Y. Yi, T. Zhang, X. Long, J. K. Li, L. X. Zhang, J. N. Wang, and S. H. Yang, "Cost-efficient clamping solar cells using candle soot for hole extraction from ambipolar perovskites," Energy Environ. Sci. 7(10), 3326–3333 (2014).
- ⁹K. Y. Yan, Z. H. Wei, J. K. Li, H. N. Chen, Y. Yi, X. L. Zheng, X. Long, Z. L. Wang, J. N. Wang, J. B. Xu, and S. H. Yang, "High-performance graphene-based hole conductor-free perovskite solar cells: Schottky junction enhanced hole extraction and electron blocking," Small 11(19), 2269–2274 (2015).
- ¹⁰Z. H. Yu, B. L. Chen, P. Liu, C. L. Wang, C. H. Bu, N. A. Cheng, S. H. Bai, Y. F. Yan, and X. Z. Zhao, "Stable organic-inorganic perovskite solar cells without hole-conductor layer achieved via cell structure design and contact engineering," Adv. Funct. Mater. 26(27), 4866–4873 (2016).
- ¹¹H. N. Chen, Z. H. Wei, H. X. He, X. L. Zheng, K. S. Wong, and S. H. Yang, "Solvent engineering boosts the efficiency of paintable carbon-based perovskite solar cells to beyond 14%," Adv. Energy Mater. 6(8), 1502087 (2016).
- ¹²X. Y. Meng, J. S. Zhou, J. Hou, X. Tao, S. H. Cheung, S. K. So, and S. H. Yang, "Versatility of carbon enables all carbon-based perovskite solar cells to achieve high efficiency and high stability," Adv. Mater. 30(21), 1706975 (2018).
- ¹³Y. Hu, Z. H. Zhang, A. Y. Mei, Y. Y. Jiang, X. M. Hou, Q. F. Wang, K. Du, Y. G. Rong, Y. H. Zhou, G. Z. Xu, and H. W. Han, "Improved performance of printable perovskite solar cells with bifunctional conjugated organic molecule," Adv. Mater. 30(11), 1705786 (2018).
- 14J. K. Du, S. Liu, J. W. Wu, W. H. Zhang, W. H. Zhang, A. Y. Mei, Y. G. Rong, Y. Hu, and H. W. Han, "Crystallization control of methylammonium-free perovskite in two-step deposited printable triple-mesoscopic solar cells," Solar RRL 4(12), 2000455 (2020).
- 15X. Y. Chen, Y. K. Xia, Q. Y. Huang, Z. Li, A. Y. Mei, Y. Hu, T. Wang, R. Cheacharoen, Y. G. Rong, and H. W. Han, "Tailoring the dimensionality of hybrid perovskites in mesoporous carbon electrodes for type-II band alignment and enhanced performance of printable hole-conductor-free perovskite solar cells," Adv. Energy Mater. 11(18), 2100292 (2021).
- ¹⁶Z. L. Ku, Y. G. Rong, M. Xu, T. F. Liu, and H. W. Han, "Full printable processed mesoscopic CH₃NH₃PbI₃/TiO₂ heterojunction solar cells with carbon counter electrode," Sci. Rep. 3, 3132 (2013).
- ¹⁷S. Liu, D. Y. Zhang, Y. S. Sheng, W. H. Zhang, Z. T. Qin, M. C. Qin, S. Li, Y. F. Wang, C. X. Gao, Q. F. Wang, Y. Ming, C. Liu, K. Yang, Q. Y. Huang, J. H. Qi, Q. J. Gao, K. Chen, Y. Hu, Y. G. Rong, X. H. Lu, A. Y. Mei a, and H. W. Han, "Highly oriented MAPbI3 crystals for efficient hole-conductor-free printable mesoscopic perovskite solar cells," Fundam. Res. 10, 276–283 (2021).
 ¹⁸T. T. Shi, S. Y. Lin, M. Fang, D. M. Kong, Y. B. Yuan, Y. L. Gao, B. C. Yang,
- H. W. Han, and C. H. Zhou, "Low-temperature fabrication of carbon-electrode based, hole-conductor-free and mesoscopic perovskite solar cells with power conversion efficiency > 12% and storage-stability > 220 days," Appl. Phys. Lett. 117(16), 163501 (2020).
- 19 D. E. Guo, J. Ma, S. Y. Lin, H. Huang, X. Guo, D. M. Kong, Y. L. Gao, W. H. Zhang, Y. Hu, and C. H. Zhou, "Sno₂ modified mesoporous $\rm ZrO_2$ as efficient electron-transport layer for carbon-electrode based, low-temperature mesoscopic perovskite solar cells," Appl. Phys. Lett. 120(26), 263502 (2022).

- ²⁰M. I. Saidaminov, A. L. Abdelhady, B. Murali, E. Alarousu, V. M. Burlakov, W. Peng, I. Dursun, L. F. Wang, Y. He, G. Maculan, A. Goriely, T. Wu, O. F. Mohammed, and O. M. Bakr, "High-quality bulk hybrid perovskite single crystals within minutes by inverse temperature crystallization," Nat. Commun. 6, 7586 (2015).
 ²¹Z. L. Chen, B. Turedi, A. Y. Alsalloum, C. Yang, X. P. Zheng, I. Gereige,
- A. AlSaggaf, O. F. Mohammed, and O. M. Bakr, "Single-crystal MAPbI₃ perovskite solar cells exceeding 21% power conversion efficiency," ACS Energy Lett. 4(6), 1258–1259 (2019).
- ²²Q. F. Wang, W. H. Zhang, Z. H. Zhang, S. Liu, J. W. Wu, Y. J. Guan, A. Y. Mei, Y. G. Rong, Y. Hu, and H. W. Han, "Crystallization control of ternary-cation perovskite absorber in triple-mesoscopic layer for efficient solar cells," Adv. Energy Mater. 10(5), 1903092 (2020).
- ²³H. N. Chen, Z. H. Wei, H. X. He, X. L. Zheng, K. S. Wong, and S. H. Yang, "Solvent effect on the hole-conductor-free fully printable perovskite solar cells," Nano Energy 27, 130–137 (2016).
- ²⁴Y. G. Rong, Z. L. Ku, A. Y. Mei, T. F. Liu, M. Xu, S. G. Ko, X. Li, and H. W. Han, "Hole-conductor-free mesoscopic TiO₂/CH₃NH₃PbI₃ heterojunction solar cells based on anatase nanosheets and carbon counter electrodes," J. Phys. Chem. Lett. 5(12), 2160–2164 (2014).
- ²⁵M. Duan, Y. G. Rong, A. Y. Mei, Y. Hu, Y. S. Sheng, Y. J. Guan, and H. W. Han, "Efficient hole-conductor-free, fully printable mesoscopic perovskite solar cells with carbon electrode based on ultrathin graphite," Carbon 120, 71–76 (2017).
- ²⁶L. J. Zhang, T. F. Liu, L. F. Liu, M. Hu, Y. Yang, A. Y. Mei, and H. W. Han, "The effect of carbon counter electrodes on fully printable mesoscopic perovskite solar cells," J. Mater. 3(17), 9165–9170 (2015).
- ²⁷J. F. Wang, S. Q. Luo, Y. Lin, Y. F. Chen, Y. H. Deng, Z. M. Li, K. Meng, G. Chen, T. T. Huang, S. Xiao, H. Huang, C. H. Zhou, L. M. Ding, J. He, J. S. Huang, and Y. B. Yuan, "Templated growth of oriented layered hybrid perovskites on 3D-like perovskites," Nat. Commun. 11(1), 582 (2020).
- ²⁸H. Chen, K. M. Li, H. Liu, Y. L. Gao, Y. B. Yuan, B. C. Yang, and C. H. Zhou, "Dependence of power conversion properties of hole-conductor-free mesoscopic perovskite solar cells on the loading of perovskite crystallites," Org. Electron. **61**, 119–124 (2018).
- 29 X. X. Ren, L. X. Zhang, Y. B. Yuan, and L. M. Ding, "Ion migration in perovskite solar cells," J. Semicond. 42(1), 010201 (2021).
- 30 D. Wei, F. S. Ma, R. Wang, S. Y. Dou, P. Cui, H. Huang, J. Ji, E. D. Jia, X. J. Jia, S. Sajid, A. M. Eiseman, L. H. Chu, Y. F. Li, B. Jiang, J. Qiao, Y. B. Yuan, and M. C. Li, "Ion-migration inhibition by the cation- π interaction in perovskite materials for efficient and stable perovskite solar cells," Adv. Mater. 30(31), 1707583 (2018).
- ³¹K. M. Li, H. Chen, H. Liu, Y. B. Yuan, Y. L. Gao, B. C. Yang, and C. H. Zhou, "Dependence of power conversion properties of the hole-conductor-free mesoscopic perovskite solar cells on the thickness of carbon film," Org. Electron. 62, 298–303 (2018).
- ³²A. Y. Mei, X. Li, L. F. Liu, Z. L. Ku, T. F. Liu, Y. G. Rong, M. Xu, M. Hu, J. Z. Chen, Y. Yang, M. Gratzel, and H. W. Han, "A hole-conductor-free, fully printable mesoscopic perovskite solar cell with high stability," Science 345(6194), 295–298, (2014).